

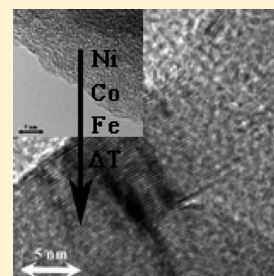
Base Metal Catalyzed Graphitization of Cellulose: A Combined Raman Spectroscopy, Temperature-Dependent X-ray Diffraction and High-Resolution Transmission Electron Microscopy Study

Jacco Hoekstra,[†] Andrew M. Beale,^{‡,§,⊥} Fouad Soulimani,[‡] Marjan Versluijs-Helder,[‡] John W. Geus,[†] and Leonardus W. Jenneskens^{*,†}

[†]Organic Chemistry and Catalysis and [‡]Inorganic Chemistry and Catalysis, Debye Institute for Nanomaterials Science, Utrecht University, Universiteitsweg 99, 3584 CG Utrecht, The Netherlands

S Supporting Information

ABSTRACT: Microcrystalline cellulose (MCC) spheres homogeneously loaded with the nitrate salts of copper, nickel, cobalt, or iron are excellent model systems to establish the temperature at which highly dispersed base metal nanoparticles are formed as well as to establish the temperature at which catalytic graphitization occurs during pyrolysis in the temperature regime $T = 500\text{--}800\text{ }^{\circ}\text{C}$. Temperature-dependent X-ray diffraction (TD-XRD) and high-resolution transmission electron microscopy (HRTEM) showed that the base metal nanoparticles are smoothly formed from related base metal oxides via carbothermal reduction (fcc copper, $T < 500\text{ }^{\circ}\text{C}$; fcc nickel, $T < 500\text{ }^{\circ}\text{C}$; fcc cobalt, $T = 570\text{ }^{\circ}\text{C}$; bcc iron, $T = 700\text{ }^{\circ}\text{C}$). Moreover, it is shown that at distinct temperatures nickel ($T \geq 800\text{ }^{\circ}\text{C}$), cobalt ($T \geq 800\text{ }^{\circ}\text{C}$), and iron ($T \geq 715\text{ }^{\circ}\text{C}$) nanoparticles catalyze the conversion of the amorphous carbon support into ribbons of turbostratic graphitic carbon according to Raman spectroscopy and TD-XRD. Copper, however, was found to be inactive. Furthermore, HRTEM revealed that nickel ($500\text{ }^{\circ}\text{C} \leq T < 800\text{ }^{\circ}\text{C}$) and cobalt nanoparticles ($700\text{ }^{\circ}\text{C} \leq T < 800\text{ }^{\circ}\text{C}$) after their initial formation become encapsulated by graphite-like shells prior to the onset of catalytic graphitization. This does not occur in the presence of iron nanoparticles. This distinction is attributed to the temperature required to access iron nanoparticles by carbothermal reduction and their concomitant mobility. Evidence (HRTEM) is provided that for the onset of catalytic graphitization nickel and cobalt nanoparticles first have to escape from their graphite-like shells. Therefore, iron nanoparticles are the most active catalyst. Our results further show that (metastable) metal carbides play a pivotal role in catalytic graphitization. This is demonstrated by the inactivity of copper nanoparticles, the distinct onset temperatures of catalytic graphitization, and the identification of cementite in the case of iron nanoparticles.



1. INTRODUCTION

Nanostructured graphitic carbon materials (NGCMs) play a key role in many applications. Examples are catalyst supports,¹ electrode materials,² fuel cells,³ and in remediation.⁴ Common preparative methods of NGCMs are laser ablation,⁵ arc discharge,⁶ and chemical vapor deposition,⁷ which require experimentally harsh conditions and which hamper large-scale synthesis. Hence, there is an ongoing search for sustainable synthetic methods for NGCM preparation that are also fit for large-scale syntheses.

Catalytic graphitization⁸ represents a way to prepare graphitic carbon under considerably more moderate conditions.^{9,10} The conversion of amorphous carbonaceous material into graphite can be lowered from ca. $T = 3200\text{ }^{\circ}\text{C}$ ¹¹ to as low as $T = 600\text{ }^{\circ}\text{C}$ by catalytic graphitization.¹² A variety of transition metals has been identified as catalysts: nickel, cobalt, and iron, which are all capable of forming (metastable) metal carbides,¹³ are used most frequently.

Two approaches are frequently applied in catalytic graphitization. In one approach, the catalytically active species is an integral part of the carbon precursor, that is, organo-metallic compounds are used that are subjected to pyrolysis.

Examples are iron- or cobalt-gluconates¹⁴ and nickel-phthalocyanines.¹⁵ The well-defined carbon source and optimal molecular dispersion of the metal species is beneficial and yields reproducible NGCMs of consistent quality. Notwithstanding, their applicability remains limited because of their relatively high cost hampering large-scale syntheses of NGCMs. In another approach, carbon sources, such as amorphous carbon films,^{16–18} polyfurfuryl alcohol,¹⁹ phenolic resins,²⁰ surfactants,²¹ and polymer spheres,^{22,23} are pyrolyzed after mixing/impregnation with commonly the nitrate salts of nickel or iron.

More recently, biomass has been identified as a potentially attractive precursor for NGCMs;⁴ it is omnipresent, environmentally benign, and cheap. Hitherto, various natural carbon precursors were investigated, such as sawdust^{24,25} and (hydrothermally treated^{26–28}) saccharides.²⁹ Furthermore, only a few papers have dealt with the metal-catalyzed graphitization of (native) cellulose.^{30–33}

Received: January 16, 2015

Revised: April 15, 2015

Published: April 15, 2015

We recently reported that microcrystalline cellulose (MCC) spheres can be loaded with base metal salts (nitrates of copper, nickel, cobalt, iron) by simple wet impregnation,³³ combining an excellent dispersion of the base metal salts, approaching that of organometallic compounds, with a cheap carbon precursor. Pyrolysis of the loaded MCC spheres gives an amorphous carbonaceous support containing well-dispersed base metal oxide nanoparticles, which at a distinct temperature are carbothermally reduced into dispersed base metal nanoparticles. Finally, catalytic graphitization of the amorphous carbonaceous support may occur in the case of base metal (nano)particles capable of forming (metastable) metal carbides.³³

Catalytic graphitization has been recognized to give NGCMs under moderate synthesis conditions. In recent literature, mostly nickel or iron catalysts have been employed in the temperature range $T = 900\text{--}1000\text{ }^{\circ}\text{C}$.^{14–33} Moreover, the emphasis in most studies has been on the formation of NGCMs and their applications. Less attention has been given to the factors controlling the efficacy of base metal catalysts particularly in the lower temperature range, namely, the onset of catalytic graphitization. This is the subject of this paper. To this end, we have pyrolyzed microcrystalline cellulose (MCC) spheres homogeneously loaded with the nitrate salts of copper, nickel, cobalt, and iron under a stagnant $\text{N}_2(\text{g})$ atmosphere in the temperature range $T = 500\text{--}800\text{ }^{\circ}\text{C}$ followed by detailed investigations with Raman spectroscopy, temperature-dependent X-ray diffraction (TD-XRD), and high-resolution transmission electron microscopy (HRTEM).

2. MATERIALS AND METHODS

Chemicals. MCC spheres (Cellets, Syntapharm GmbH, Mülheim an der Ruhr, Germany, size $100\text{--}200\text{ }\mu\text{m}$) were used as substrate. $\text{Cu}(\text{NO}_3)_2 \cdot 2.5\text{H}_2\text{O}$, $\text{Ni}(\text{NO}_3)_2 \cdot 6\text{H}_2\text{O}$, $\text{Co}(\text{NO}_3)_2 \cdot 6\text{H}_2\text{O}$, and $\text{Fe}(\text{NO}_3)_3 \cdot 9\text{H}_2\text{O}$ were purchased from Sigma-Aldrich (>98% purity).

Preparation.³³ MCC spheres (50.0 g) were immersed for 24 h in 2.0 M aqueous solutions (100 mL) of the respective nitrate metal salts under occasional stirring, collected by filtration (Büchner funnel with glass filter) and dried in vacuo ($p = 10^{-2}$ mbar) at room temperature to constant weight.

Samples (5.0 g) of either pristine MCC spheres or the dried loaded spheres were pyrolyzed in a stagnant $\text{N}_2(\text{g})$ atmosphere in a horizontally placed quartz glass tube of a tube furnace reactor (TFR, Thermolyne 21100 furnace). Prior to pyrolysis, the reactor was evacuated and refilled with $\text{N}_2(\text{g})$ three times. Next, the TFR was heated (rate $5\text{ }^{\circ}\text{C}\cdot\text{min}^{-1}$) to the desired final temperature, namely, $T = 500, 600, 700$, or $800\text{ }^{\circ}\text{C}$ followed by isothermal pyrolysis for 3 h (see also Table S1 of the Supporting Information).

Characterization. An FEG Tecnai-20 transmission electron microscope ((HR)TEM, FEI), operated at 200 kV, equipped with a field-emission gun supplied information about the structure of the carbon materials. The samples were prepared by grinding and ultrasonic dispersion in ethanol. A drop of the suspension was applied onto a holey carbon film on top of a copper grid. A CCD camera at the bottom of the microscope was employed to obtain HRTEM images exhibiting lattice images.

Powder X-ray diffraction (XRD) patterns were obtained from $2\theta = 25\text{--}80^{\circ}$ with a Bruker-AXS X-ray diffractometer equipped with an Anton-Paar XRK reaction chamber using $\text{Co K}_{\alpha 12}$ radiation ($\lambda = 0.17902\text{ nm}$). The samples were heated in a

$\text{He}(\text{g})$ flow ($20\text{ L}\cdot\text{h}^{-1}$) to $T = 800\text{ }^{\circ}\text{C}$ (heating rate $5\text{ }^{\circ}\text{C}\cdot\text{min}^{-1}$) and were kept at $T = 800\text{ }^{\circ}\text{C}$ for 1 h. The Bragg equation (eq 1) was used to calculate the $d(002)$ interlayer spacing between graphitic layers: $d(002) = \lambda/2\sin\theta$ (eq 1), in which $d(002)$ is the interlayer spacing, λ is the wavelength of the $\text{CoK}_{\alpha 12}$ radiation, and θ is the Bragg angle.

Metal loadings were determined using an IRIS intrepid II XSP inductively coupled plasma mass spectrometer (ICP-MS). The carbon support was stepwise gasified after which the resulting metal was dissolved in HNO_3 ($T = 80\text{ }^{\circ}\text{C}$). During isothermal pyrolysis at a designated temperature, namely, $T = 500, 600, 700$, or $800\text{ }^{\circ}\text{C}$, the loss of carbonaceous material from both the pristine and the loaded MCC spheres increases concomitant with an increase in temperature.³³ Therefore, an increase of metal content (wt %) is observed for the loaded MCC with increasing temperature (Table S1 of the Supporting Information). In all pyrolysis experiments, samples (5.0 g) of either pristine MCC spheres or dried loaded MCC spheres were used.

Raman spectra were recorded using a $\lambda\text{ }532\text{ nm}$ (2.33 eV) diode laser operating at 35 mW and a Holoprobe Kaiser optical spectrometer equipped with a holographic notch filter and CCD camera. Data were collected for 30 s over a range of $300\text{--}4300\text{ cm}^{-1}$ (resolution 6 cm^{-1}).

Deconvolution. The Raman spectra were analyzed using GRAMS/AI software. A multipoint manual baseline subtraction was performed over the entire spectra, and curve fitting of the Raman peaks was done using the Levenberg–Marquardt algorithm. Peak fitting was performed using mainly Lorentzian functions; only one broad band positioned at ca. 1500 cm^{-1} appeared to be best approximated using a Gaussian function (Table S2 of the Supporting Information). A similar deconvolution protocol was validated and applied by Sadezky et al. in the deconvolution of a large number of Raman spectra of soot.³⁴ To ensure an optimal fit of the data, the spectra were delineated and fitted separately in the first-order region ($800\text{ cm}^{-1}\text{--}1900\text{ cm}^{-1}$) and the second-order region ($2100\text{--}3500\text{ cm}^{-1}$). The first-order region was best fitted with either five or six bands. One band, denoted B, represented an artifact of the instrumental setup and was not related to the carbon species. The second-order region was best fitted with four bands. When fitting the data, one band in the first-order region (1500 cm^{-1}) and one band in the second-order region (2700 cm^{-1}) were constrained to remain within ca. 50 cm^{-1} of their original position. The reduced χ^2 value was used to determine an optimal fit to the data and in all cases was below 2%.

3. RESULTS AND DISCUSSION

Loaded MCC spheres were prepared by wet impregnation using 2.0 M aqueous solutions (100 mL) of the respective metal nitrate (copper, nickel, cobalt, or iron) salts. After workup and drying to constant weight, the loaded MCC spheres were pyrolyzed in a stagnant $\text{N}_2(\text{g})$ atmosphere using a TFR (heating rate $5\text{ }^{\circ}\text{C}\cdot\text{min}^{-1}$) to the desired final temperature, namely, $T = 500, 600, 700$, or $800\text{ }^{\circ}\text{C}$, followed by isothermal pyrolysis for 3 h (see Materials and Methods).³³ Because evidence is available that (metastable) metal carbides play a decisive role as intermediates in catalytic graphitization,³⁵ we have also included MCC spheres loaded with dispersed copper nanoparticles. Whereas nickel, cobalt, and iron are capable of (metastable) metal carbide formation,¹³ this is not the case for copper.^{33,35} Furthermore, we have also subjected pristine MCC spheres to similar pyrolysis conditions. All samples were studied

using Raman spectroscopy, temperature-dependent X-ray diffraction (TD-XRD), and high-resolution transmission electron microscopy (HRTEM) in the temperature range $T = 500\text{--}800\text{ }^{\circ}\text{C}$ to gain insight in the factors controlling particularly the onset of catalytic graphitization.

Pyrolysis of MCC. The pyrolytic conversion of pristine MCC spheres to an amorphous carbonaceous support material in the absence of catalytic additives was investigated first in order to elucidate the effect of thermal treatment on the resulting carbonaceous material.

The TD-XRD patterns (Figure 1A) are characterized by two broad reflections. The $d(002)$ reflection at $\text{ca. } 2\theta = 27^{\circ}$

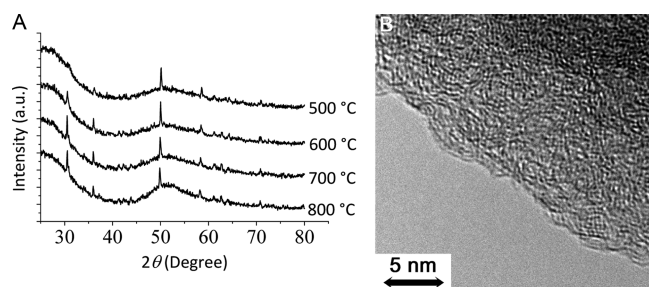


Figure 1. TD-XRD patterns of MCC beads (A, left) and HRTEM image of an amorphous carbonaceous material obtained upon pyrolysis of MCC at $T = 800\text{ }^{\circ}\text{C}$ (B, right).

corresponds to the stacking structure of graphitic carbon, and the $d(100)$ reflection at $\text{ca. } 2\theta = 51^{\circ}$ corresponds to the 2-dimensional graphitic lattice peak.^{36,37} The broadness of these reflections point to a highly disordered amorphous carbonaceous material. The sharp spikes on the diffractograms are attributed to background signals of the sample holder. The $d(002)$ interlayer spacing between the graphitic layers was calculated to be $3.83\text{ }\text{\AA}$ (Bragg equation, eq 1, Materials and Methods). Crystalline 3D-graphite, that is, highly oriented pyrolytic graphite (HOPG)¹⁹ with graphitic layers stacked in an AB fashion (Bernal structure), possesses a $d(002)$ interlayer spacing of $3.35\text{ }\text{\AA}$.³⁸ Thus, the large interlayer spacing obtained here indicates that stacking is less dense in line with the formation of an amorphous carbonaceous material.

HRTEM supports the XRD results. Figure 1B shows an HRTEM image of the carbonaceous material obtained from the pyrolysis of MCC at $T = 800\text{ }^{\circ}\text{C}$. It represents a typical image of an amorphous carbonaceous material; highly disordered nanosized crystallites are found in which stacking of graphitic layers is virtually absent.

To gain more insight in the short-range ordering, the microstructural evolution of the carbon materials obtained from MCC as a function of pyrolysis temperature was studied using Raman spectroscopy (Figure 2A).

The Raman signals of graphite result from lattice vibrations and are affected by the degree of structural disorder.³⁴ To consider the contribution of the respective bands to the Raman spectra, deconvolution is required (see Materials and Methods). Figure 2B and C shows the first- ($800\text{--}1900\text{ cm}^{-1}$) and second-order ($2100\text{--}3500\text{ cm}^{-1}$) regions of the Raman spectra of the carbonaceous material obtained from the pyrolysis of MCC at $T = 500\text{ }^{\circ}\text{C}$ with their respective curve fits.

The first-order spectrum is dominated by two broad peaks. The band positioned at 1594 cm^{-1} is the so-called G- (graphitic) band.³⁹ It corresponds to an ideal graphitic lattice vibration and involves the in-plane bond stretching motion of

pairs of sp^2 hybridized carbon atoms (Figure S1 of the Supporting Information).⁴⁰ In the case of crystalline graphite (e.g., HOPG), the G-band is positioned at 1580 cm^{-1} . A shift to higher wavenumbers has been observed for very small or disordered crystallites with little three-dimensional order.^{41,42} The reason for this shift is the contribution of a low-intensity Raman band positioned around 1615 cm^{-1} (D2), which is attributed to the edges of graphitic crystallites.⁴³ If the size of a graphitic crystallite decreases, the proportion of edges will increase and, consequently, the D2 band will become more dominant. The nanosized graphitic crystallites, such as those shown in Figure 1B, will have a high proportion of edges. In this case, the D2-band will broaden to such an extent that it becomes more convenient to consider a single G/D2 combination band. Because the G- and D2-bands are fitted as a single peak, a net shift in the position of this band toward the higher wavenumber position of the D2-band is found with respect to that found for highly crystalline graphite. Whereas an ordered graphitic sample exhibits only the G-band, distorted graphite shows additional bands. The most intense of these additional bands, denoted as D1, will be positioned near 1360 cm^{-1} and is characteristic for the in-plane breathing vibrations of sp^2 -bonded carbon within structural defects (Figure S1 of the Supporting Information).⁴⁰ This band is prominent in disordered graphitic samples and is indicative for the presence of edges of the graphitic crystallites. It is already observed at crystallite sizes below 100 nm .^{34,39} The D3-band in between the D1- and G-band centered at $1500\text{--}1550\text{ cm}^{-1}$ stems from an amorphous carbon phase.^{44,45} Around 1200 cm^{-1} , a hidden band is found as a shoulder of the D1-band. This D4-band is ascribed to either $\text{sp}^2\text{--sp}^3$ bonds or C–C and C=C stretching vibrations of polyenes.⁴⁶ An additional background peak was found around 1000 cm^{-1} , which represents an artifact of the experimental setup. It was taken into consideration with the deconvolution procedure; it is denoted as B (Table S2 of the Supporting Information).

The second-order Raman spectrum ($2100\text{--}3500\text{ cm}^{-1}$, Figure 2C) shows broad bands which are generally observed for disordered carbons. The signals are attributed to overtones and combinations of graphite vibrations.⁴⁴ The band at 2900 cm^{-1} is assigned to the G + D1 overtone combination. Shoulders at 3100 and 2400 cm^{-1} are assigned to $2 \times \text{D2}$ and $2 \times \text{D4}$ overtones. Special attention is drawn to the peak at 2700 cm^{-1} , which is an overtone of the D1-band. For an isolated graphene sheet, the $2 \times \text{D1}$ band is a single peak. When the number of graphitic layers increase (2–4, Bernal structure³⁸), the $2 \times \text{D1}$ band splits into multiple bands because of symmetry changes. For larger graphitic crystallites, the band eventually evolves into a double band.⁴⁷

The first-order Raman spectra of the amorphous carbonaceous material obtained by the pyrolysis of pristine MCC in the temperature range $T = 500\text{--}800\text{ }^{\circ}\text{C}$ undergo only minor changes with temperature (Figure 2A). The deconvolution results are summarized in Table S3 of the Supporting Information. With increasing temperature, the position of the D1-band shifts to lower wavenumbers (from 1374 to 1336 cm^{-1}). The full width at half-maximum (fwhm) of the D1-band narrows from 158 to 148 cm^{-1} , which indicates that the crystallite sizes of the amorphous carbons are very small (nanometer range) and display a wide size distribution. The fwhm of the G/D2-band also narrows (from 82 to 56 cm^{-1}); however, because of the merging of the G and D2 band (vide supra), this signal is fairly broad. The modest narrowing of both

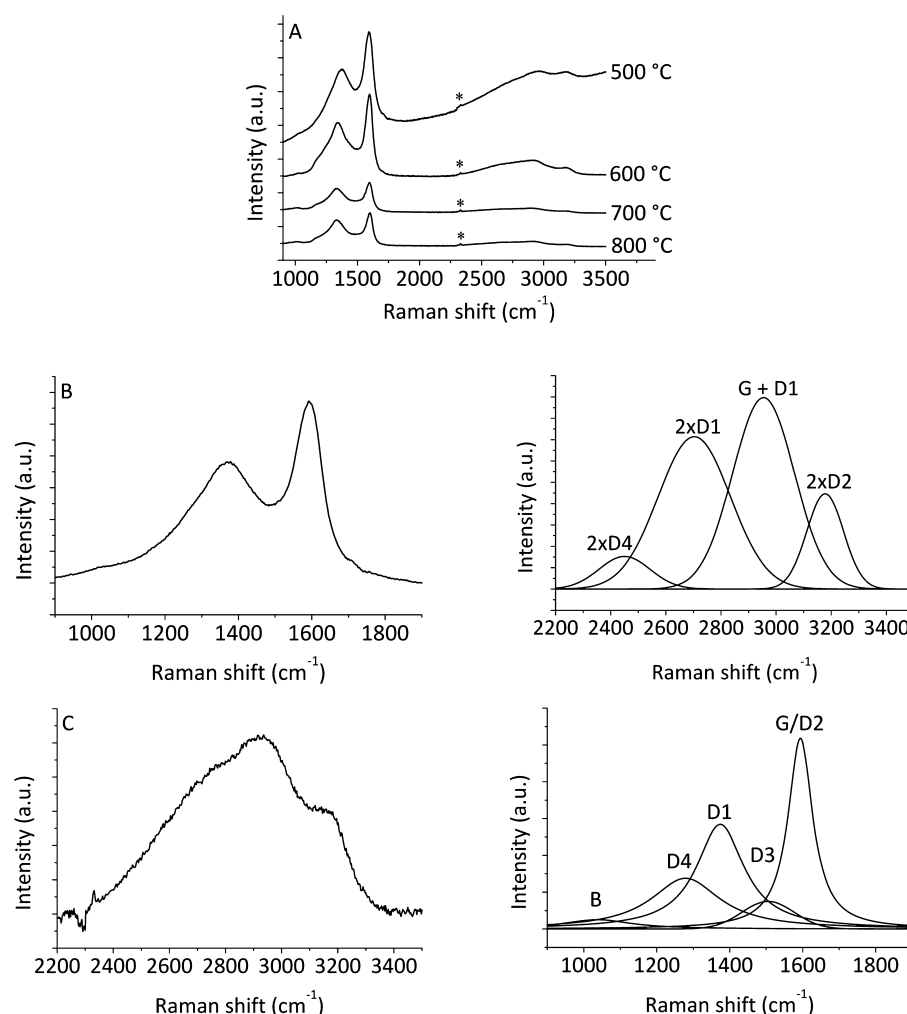


Figure 2. (A) Raman spectra of the amorphous carbonaceous materials obtained; (B) magnification of the first-order Raman spectrum and deconvolution ($T = 500\text{ }^{\circ}\text{C}$); (C) magnification of the second-order Raman spectrum and deconvolution ($T = 500\text{ }^{\circ}\text{C}$). *, $\text{N}_2(\text{g})$.

bands indicates a slight ordering of the amorphous carbons with an increase of temperature. The second-order spectrum verifies these results. The $2 \times \text{D1}$ band remains broad ($\text{fwhm} = \text{ca. } 308\text{ cm}^{-1}$) throughout the whole temperature range which is indicative for the presence of amorphous carbonaceous material.

The carbonization of MCC in the temperature range $T = 500\text{--}800\text{ }^{\circ}\text{C}$ in the absence of catalytic additives thus results in the formation of an amorphous carbon. This is consistent with literature data in which the carbonization of MCC in the temperature range $T = 250\text{--}1000\text{ }^{\circ}\text{C}$ has been investigated.^{48,49} Nanosized crystalline sp^2 hybridized carbon clusters were formed in a disordered matrix of both amorphous sp^3 - and sp^2 -hybridized carbon. Limited growth of these clusters occurred up until $T = 1000\text{ }^{\circ}\text{C}$; however, the size of these clusters remained within the nanometer dimensions.

Catalytic Graphitization. During pyrolysis of the loaded MCC bodies, catalytic graphitization was only observed in the presence of nickel-, cobalt-, and iron-nanoparticles.³³ Catalytic graphitization was not discernible in the presence of copper-nanoparticles. This has been attributed to the low solubility of carbon in copper, that is, copper does not readily form (metastable) copper carbides (vide infra).³⁵

Copper. Therefore, we also analyzed the influence of copper nanoparticles on the amorphous carbonaceous support

obtained after pyrolysis at $T = 500, 600, 700$, and $800\text{ }^{\circ}\text{C}$. TD-XRD revealed that the dispersed copper salt precursors are carbothermally reduced to fcc copper nanoparticles already at $T < 500\text{ }^{\circ}\text{C}$. In the whole temperature range ($T = 500\text{--}800\text{ }^{\circ}\text{C}$), no evidence for the formation of graphitic species was found using TD-XRD (absence of $d(002)$ reflection: Figure S2 of the Supporting Information). TEM and HRTEM showed that the copper nanoparticles remain embedded in an amorphous carbonaceous matrix (Figure S3 of the Supporting Information). This is further substantiated by the Raman spectra of the samples after pyrolysis at $T = 500, 600, 700$, and $800\text{ }^{\circ}\text{C}$ (Figure S4 and Table S4 of the Supporting Information). Deconvolution gave the same number of bands, band positions, and fwhm 's as found for the pyrolyzed samples of pristine MCC (Table S3 of the Supporting Information). Hence, in agreement with available data,³⁵ copper is inactive in catalytic graphitization in the temperature range investigated (Figures S2–S4 and Table S4 of the Supporting Information).

Nickel. With TD-XRD, it was found that the nickel salt became reduced below $T = 500\text{ }^{\circ}\text{C}$.³³ Around $T = 800\text{ }^{\circ}\text{C}$, a weak reflection in the XRD pattern is observed at $2\theta = 30.2^{\circ}$ attributed to $d(002)$ of graphite (Figure 3) with an interlayer spacing of 3.44 \AA (calculated using Bragg's law, eq 1, Materials and Methods). This interlayer spacing is significantly smaller than that of the original amorphous carbon bodies derived from

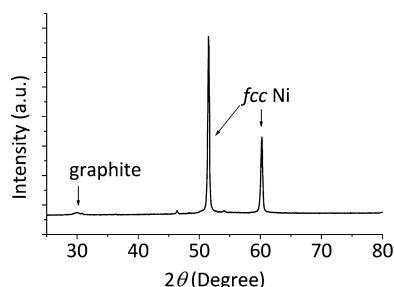


Figure 3. XRD pattern of carbon-supported fcc nickel nanoparticles after pyrolysis at $T = 800\text{ }^{\circ}\text{C}$.

pristine MCC ($3.83\text{ }\text{\AA}$, vide supra). Notwithstanding, it is still larger than that of crystalline graphite ($3.35\text{ }\text{\AA}$) with a Bernal structure. By definition, when the interlayer spacing between adjacent graphitic layers exceeds $3.42\text{ }\text{\AA}$, a so-called turbostratic stacking is found,³⁸ which means that the stacking is rotationally random. At lower temperatures, graphite formation is not observed with XRD.

With HRTEM, however, graphite-like material is observed already after treatment at $T = 500\text{ }^{\circ}\text{C}$ (Figure 4A). The nickel

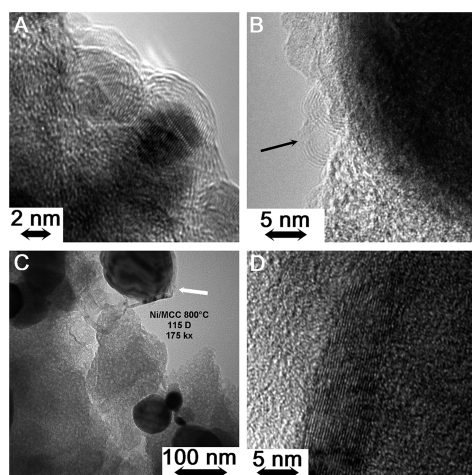


Figure 4. (A) HRTEM image of a nickel nanoparticle encapsulated in a graphite-like envelope obtained after pyrolysis at $T = 500\text{ }^{\circ}\text{C}$, (B) HRTEM image of a broken graphite-like shell after pyrolysis at $T = 800\text{ }^{\circ}\text{C}$, (C) TEM image of graphitic nanoribbons ($T = 800\text{ }^{\circ}\text{C}$), and (D) HRTEM image of the stacking of the graphitic layers ($T = 800\text{ }^{\circ}\text{C}$).

nanoparticles are encapsulated in a few graphite-like shells. The temperature at which the graphite-like shells are formed ($T < 500\text{ }^{\circ}\text{C}$) suggests that nickel carbide (Ni_3C) was involved in its formation. The nickel nanoparticles are capable to take up carbon atoms from the amorphous carbon forming metastable Ni_3C . Because graphitic carbon is thermodynamically more stable than Ni_3C , carbon will subsequently segregate as a graphite-like shell on the surface of the nickel particles. This is in line with the preparation of spherical nanoshells of graphite-like carbon⁵⁰ by heating Ni_3C nanoparticles just above their decomposition temperature ($T = 420\text{ }^{\circ}\text{C}$),^{13,51} similar to the graphite-like shells here observed. Apparently, these small graphitic domains are not large enough to be visualized with XRD, particularly in the presence of the crystalline fcc nickel nanoparticles.

Nickel possesses a higher thermal expansion coefficient than its surrounding graphite-like shell (ca. twice as high, Table S8 of the Supporting Information).⁵² Hence, with increasing temperatures, the nickel nanoparticles will develop pressure via expansion onto the inner surface of their surrounding graphite-like shell. As a consequence, the nickel nanoparticles can break the shell and pass through the graphitic layers. The arrow in Figure 4B points to a broken shell; a magnification is provided (Figure S8 of the Supporting Information). The nickel nanoparticle is then forced to flow out and can migrate to another patch of the amorphous carbon where it can start to recrystallize the available amorphous carbonaceous support material to graphitic carbonaceous material. This process starts around $T = 800\text{ }^{\circ}\text{C}$. This is also in agreement with the results of an in-situ XRD study of the catalytic graphitization of amorphous carbon/nickel bilayers deposited onto a SiO_2 substrate upon heating at $T = 900\text{ }^{\circ}\text{C}$ or $T = 1000\text{ }^{\circ}\text{C}$ by rapid thermal annealing (heating rate $35\text{ }^{\circ}\text{C s}^{-1}$) under inert conditions.⁵³ They also found an onset of catalytic graphitization at ca. $T = 800\text{ }^{\circ}\text{C}$ for nickel nanoparticles with an average diameter of 30 nm , which is close to the 40 nm found in our case.³³ The TEM image (Figure 4C) clearly shows the origin of the graphite reflection in the XRD pattern. Close to the nickel particle (top right, indicated with an arrow), a ribbon is observed. The HRTEM image (Figure 4D) shows that this ribbon consists of straight stacked graphitic layers stressing that this graphitic domain was not formed during encapsulation of a nickel nanoparticle, otherwise a much more curved structure would be observed. Notwithstanding, the total amount of graphitic nanoribbons throughout the sample loaded with nickel after pyrolysis at $T = 800\text{ }^{\circ}\text{C}$ remains low.

Although with HRTEM some graphite-like material was already found after treatment at $T = 500\text{ }^{\circ}\text{C}$, with Raman spectroscopy no significant difference is observed between the carbon materials obtained in the absence and presence of nickel in the temperature range $T = 500\text{--}700\text{ }^{\circ}\text{C}$ (Figure S5 and Table S5 of the Supporting Information). Only the shift of the D1-band after treatment at $T = 500\text{ }^{\circ}\text{C}$ to lower wavenumber indicates some ordering. This is attributed to the fact that also a significant amount of amorphous carbonaceous material remains present which is also Raman active. At $T = 800\text{ }^{\circ}\text{C}$, however, a marked difference is detected (Figure 5). A modest

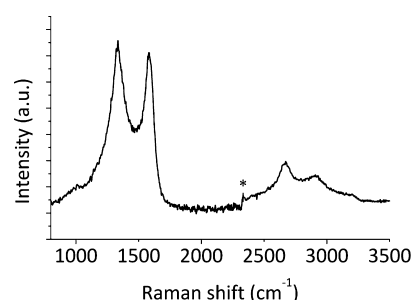


Figure 5. Raman spectrum of nickel-loaded MCC beads after pyrolysis at $T = 800\text{ }^{\circ}\text{C}$. *, $\text{N}_2(\text{g})$.

narrows of the D1 band is observed (see also Table S5 of the Supporting Information). The most striking change is found in the second-order Raman spectrum. Particularly, the $2 \times \text{D1}$ band situated at 2670 cm^{-1} becomes more prominent and sharpens ($\text{fwhm} = 127\text{ cm}^{-1}$ vs 310 cm^{-1} for the pyrolyzed pristine MCC series, Table S3 of the Supporting Information).

For highly crystalline graphite, a double band would have been expected as discussed above. The observation of only a single band is attributed to the turbostratic stacking of the graphitic material. Because there is no interlayer interaction between the adjacent graphitic layers, the Raman spectrum resembles that of monolayer graphene.³⁸ The broadening of the $2 \times \text{D1}$ band has been observed before for turbostratic graphite, although to a lesser extent ($45\text{--}60\text{ cm}^{-1}$)⁵⁴ than in our case. This is attributed to the fact that our samples consist of a mixture of amorphous, graphite-like, and graphitic carbon which are all Raman active.

Cobalt. TD-XRD experiments revealed that cobalt was fully reduced at $T = 570\text{ }^{\circ}\text{C}$. Encapsulation of the fcc cobalt nanoparticles with thin graphite-like shells was observed at $T = 700\text{ }^{\circ}\text{C}$,³³ similar to the nickel nanoparticles, albeit at a higher temperature.

At $T = 800\text{ }^{\circ}\text{C}$, a maximum of the $d(002)$ graphite reflection appeared with a more pronounced intensity than in the case of nickel (Figure 6), the position of which again indicates a

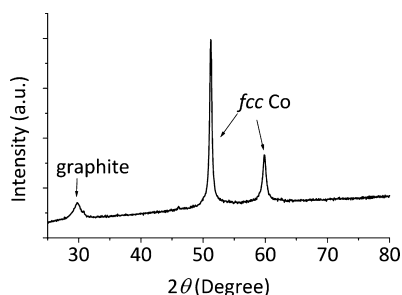


Figure 6. XRD pattern of carbon-supported fcc cobalt nanoparticles after pyrolysis at $T = 800\text{ }^{\circ}\text{C}$.

deviation from HOPG with an interlayer spacing of 3.44 Å . Consequently similar to the nickel nanoparticles, the cobalt nanoparticles have to escape from their graphite-like shell because of a higher thermal expansion of the cobalt core compared to that of the graphite-like shell (Table S8 of the Supporting Information), and they start to recrystallize the remaining amorphous carbonaceous support material at ca. $T = 800\text{ }^{\circ}\text{C}$. Likely, (metastable) cobalt carbides (Co_2C , Co_3C)³⁵ are active in this process. The thermal decomposition temperature of the cobalt carbides is near $T = 485\text{ }^{\circ}\text{C}$,¹³ a temperature at which the cobalt nanoparticles are not yet fully reduced. Upon reduction, it is assumed that the (metastable) cobalt carbides can be formed, which, similar to nickel, decompose as graphite-like shells.

With TEM, graphitic carbon with a ribbon morphology is observed upon pyrolysis of the cobalt-loaded beads at $T = 800\text{ }^{\circ}\text{C}$ (Figure 7A). The graphitic nanoribbon is much thicker

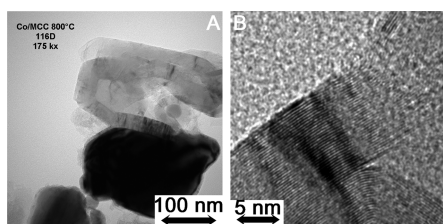


Figure 7. (A) TEM image and (B) HRTEM image of a graphitic nanoribbon obtained after pyrolysis of cobalt-loaded MCC beads at $T = 800\text{ }^{\circ}\text{C}$.

compared to the ribbons obtained with nickel (compare with Figure 4C and D). The HRTEM image (Figure 7B) shows a nanoribbon of approximately 15 nm in thickness. With cobalt, also more graphitic carbon is detected throughout the sample compared to the nickel series pyrolyzed at $T = 800\text{ }^{\circ}\text{C}$.

In Figure 8, the Raman spectrum is shown of the cobalt-loaded sample after pyrolysis at $T = 800\text{ }^{\circ}\text{C}$. Again, the D1

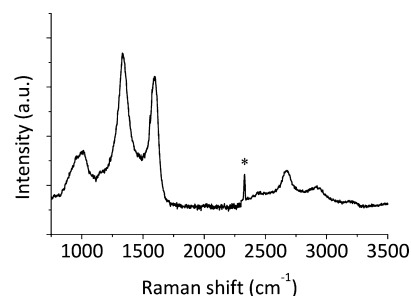


Figure 8. Raman spectrum of cobalt-loaded MCC beads after pyrolysis at $T = 800\text{ }^{\circ}\text{C}$. *, $\text{N}_2(\text{g})$.

band narrows with respect to the pristine beads. Particularly, the $2 \times \text{D1}$ band becomes more pronounced with an fwhm of 106 cm^{-1} (Figure S6 and Table S6 of the Supporting Information). This single band is again representative for a turbostratic stacking of the obtained graphitic material. It was impossible to obtain Raman spectra of the cobalt series pyrolyzed at $T = 500\text{ }^{\circ}\text{C}$ and at $T = 600\text{ }^{\circ}\text{C}$ because of severe heating of the samples. This is attributed to overlap of the laser wavelength ($\lambda\ 532\text{ nm}$, 2.33 eV) with an optical band gap of Co_3O_4 nanoparticles.⁵⁵

Iron. Pyrolysis of iron-loaded MCC spheres gives Fe_3O_4 nanoparticles on an amorphous carbonaceous support. The Fe_3O_4 nanoparticles are then stepwise reduced via FeO to bcc $\text{Fe}(0)$.³³ Immediate recrystallization of the carbon support upon the final reduction step then occurs (ca. $T = 715\text{ }^{\circ}\text{C}$) as observed with the appearance of the $d(002)$ graphitic peak at $2\theta = 30.2^{\circ}$ with TD-XRD (Figure 9). This points to the

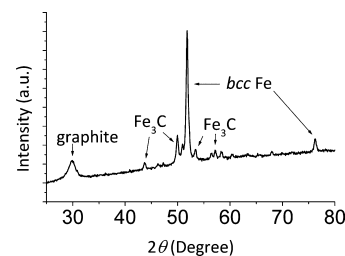


Figure 9. XRD pattern of carbon-supported bcc iron nanoparticles after pyrolysis at $T = 715\text{ }^{\circ}\text{C}$.

presence of turbostratic graphite with a 3.44 Å interlayer spacing. Catalytic graphitization occurs at a lower temperature than with nickel and cobalt ($T = 715\text{ }^{\circ}\text{C}$ vs $T = 800\text{ }^{\circ}\text{C}$). Furthermore, catalytic graphitization of the amorphous carbon appears to be a fairly quick process.⁵³ Once the $d(002)$ reflection appears, no additional changes occur as a function of time/increasing temperature. The presence of cementite (Fe_3C) in the XRD pattern suggests that (metastable) iron carbides are active in the catalytic graphitization process. The decomposition temperature of Fe_3C is $T = 700\text{ }^{\circ}\text{C}$,¹³ which is similar to the temperature of reduction of the iron oxide (FeO)

to metallic iron (Fe(0)) and is in line with the temperature at which graphite formation is observed.

Figure 10A shows a TEM image of the graphitic material obtained during pyrolysis of iron-loaded MCC beads at $T =$

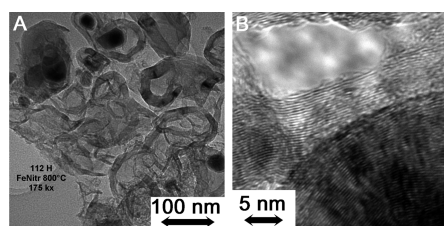


Figure 10. (A) TEM image and (B) HRTEM image of graphitic material obtained after pyrolysis of iron-loaded beads at $T = 800\text{ }^{\circ}\text{C}$.

$800\text{ }^{\circ}\text{C}$. Graphitic carbon with a ribbon morphology is produced from the amorphous carbon. The original amorphous carbonaceous material is virtually absent; almost all amorphous carbon is converted to graphitic material as shown in Figure 10B (HRTEM).

The Raman results of the iron-loaded samples strongly designate the formation of small graphitic crystallites. Figure 11A shows the Raman spectrum of the iron-loaded MCC beads after pyrolysis at $T = 800\text{ }^{\circ}\text{C}$. The D1-band at 1344 cm^{-1} is narrow (fwhm = 66 cm^{-1}), and especially, the second-order $2 \times$ D1 overtone is very intense with a low fwhm of 90 cm^{-1} (Figure S7 and Table S7 of the Supporting Information) with the single peak again being indicative for the turbostratic stacking obtained. In Figure 11B, a magnification of the G-band is shown. Both the position at 1582 cm^{-1} and the shoulder at 1616 cm^{-1} indicate the formation of the graphitic nanoribbons; the D2-band is attributed to the presence of the edges of the graphitic nanoribbons. Because the proportion of edges in the obtained graphitic nanoribbons is significantly lower with respect to the original amorphous carbon, the G-band is now more pronounced. A better fit is now obtained when the G- and D2-bands are considered separately.

Encapsulation of the iron nanoparticles with graphite-like shells, in contrast to nickel and cobalt nanoparticles, is not observed (vide supra). We propose that because of the encapsulation of nickel and cobalt at lower temperatures the catalytic graphitization process is less efficient since it will be more difficult to recrystallize the already graphite-like material present. Iron, being reduced at a higher temperature, will be too mobile at the temperature of reduction. Hence, encapsulation with a thin graphite-like shell does not occur but immediately

leads to iron-induced catalytic graphitization. This makes iron the most active catalyst.

4. CONCLUSIONS

Graphitic nanostructures were obtained from MCC spheres homogeneously loaded with the nitrate salts of nickel, cobalt, or iron after pyrolysis via metal-induced catalyzed graphitization.³³ It is shown that the amorphous carbonaceous support material obtained from the pyrolysis of MCC is converted to turbostratic graphitic carbon with a ribbon morphology under the influence of nickel, cobalt, and, especially, iron. Copper is found to be completely inactive.^{33,35} Whereas iron nanoparticles are found to be the most active catalyst at the lowest temperature ($T \geq 715\text{ }^{\circ}\text{C}$), the nickel and cobalt nanoparticles are only active in catalyzed graphitization at $T \geq 800\text{ }^{\circ}\text{C}$ with cobalt being more active than nickel. This is attributed to the observation that the nickel and cobalt nanoparticles are initially encapsulated by several thin graphite-like shells (HRTEM).³³ Hence, these metal nanoparticles have to escape from these shells before they can participate in metal-induced catalytic graphitization of still available amorphous carbon. This is facilitated by the higher thermal expansion coefficients of nickel and cobalt, which both are approximately twice as large as that of graphite at $T \geq 800\text{ }^{\circ}\text{C}$.⁵² Consequently, the nickel and cobalt nanoparticles are capable to rupture the graphite-like shells, to flow out, and to initiate catalytic graphitization of available amorphous carbon. With iron nanoparticles, encapsulation does not occur. Because the reduction to iron requires a higher temperature ($T \geq 715\text{ }^{\circ}\text{C}$), the iron nanoparticles are too mobile to become encapsulated and, hence, are immediately active in catalytic graphitization. The temperatures at which the graphite-like shells or turbostratic graphitic nanoribbons are formed provide strong evidence that (metastable) metal carbides play a pivotal role in the catalytic graphitization process.

■ ASSOCIATED CONTENT

■ Supporting Information

Molecular graphitic vibrations (Figure S1). TD-XRD (Figure S2) and (HR)TEM (Figure S3) of copper-loaded beads treated at $T = 800\text{ }^{\circ}\text{C}$. Raw Raman spectra (Figures S4–S7). Magnification of Figure 4B (Figure S8). Yields and metal loadings determined with ICP-MS (Table S1). Band positions and line shapes of the deconvolution protocol (Table S2). Deconvolution results (Tables S3–S7). Thermal expansion coefficients of the elements under survey (Table S8). The Supporting Information is available free of charge on the ACS Publications website at DOI: 10.1021/acs.jpcc.5b00477.

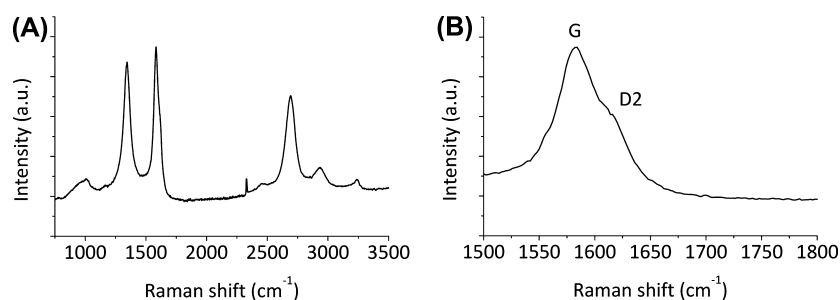


Figure 11. (A) Raman spectrum of iron-loaded MCC beads after pyrolysis at $T = 800\text{ }^{\circ}\text{C}$ and (B) magnification of the G-band. The D2-band is observed as a shoulder at 1616 cm^{-1} .

■ AUTHOR INFORMATION

Corresponding Author

*E-mail: l.w.jenneskens@uu.nl. Phone: +31 30 253 3218. Fax: +31 30 252 3615.

Present Addresses

[§]UK Catalysis Hub, Research Complex at Harwell, Rutherford Appleton Laboratory, Harwell, Didcot, Oxfordshire, OX11 0FA, United Kingdom.

[†]Department of Chemistry, University College London, 20 Gordon Street, London WC1H 0AJ, United Kingdom.

Author Contributions

The manuscript was written through contributions of all authors. All authors have given approval to the final version of the manuscript.

Notes

The authors declare no competing financial interest.

■ ACKNOWLEDGMENTS

An anonymous reviewer is acknowledged for bringing to our attention several relevant references. Agentschap NL is acknowledged for financial support (in-situ H₂O₂ project, no. IS043063).

■ REFERENCES

- (1) De Jong, K. P.; Geus, J. W. Carbon Nanofibers: Catalytic Synthesis and Applications. *Catal. Rev. Sci. Eng.* **2000**, *42*, 481–510.
- (2) McCreery, R. L. Advanced Carbon Electrode Materials for Molecular Electrochemistry. *Chem. Rev.* **2008**, *108*, 2646–2687.
- (3) Hyeon, T.; Han, S.; Sung, Y. E.; Park, K. W.; Kim, Y. W. High-Performance Direct Methanol Fuel Cell Electrodes using Solid-Phase Synthesized Carbon Nanocoils. *Angew. Chem., Int. Ed.* **2003**, *42*, 4352–4356.
- (4) Dodson, J. R.; Parker, H. L.; Garcia, A. M.; Hicken, A.; Asemave, K.; Farmer, T. J.; He, H.; Clark, J. H.; Hunt, A. J. Bio-Derived Materials as a Green Route for Precious & Critical Metal Recovery and Re-Use. *Green Chem.* **2015**, *117*, 1951–1965 DOI: 10.1039/c4gc02483d.
- (5) Guo, T.; Nikolaev, P.; Rinzler, A. G.; Tomanek, D.; Colbert, D. T.; Smalley, R. E. Self-Assembly of Tubular Fullerenes. *J. Phys. Chem. C* **1995**, *99*, 10694–10697.
- (6) Iijima, S. Helical Microtubules of Graphitic Carbon. *Nature* **1991**, *354*, 56–58.
- (7) Jose-Yacaman, M.; Miki-Yoshida, M.; Rendon, L.; Santiesteban, J. G. Catalytic Growth of Carbon Microtubules with Fullerene Structure. *Appl. Phys. Lett.* **1993**, *62*, 657–659.
- (8) Fitzer, E.; Kochling, K.-H.; Boehm, H. P.; Marsh, H. Recommended Terminology for the Description of Carbon as a Solid. *Pure Appl. Chem.* **1995**, *67*, 473–506.
- (9) Derbyshire, F. J.; Presland, A. E. B.; Trimm, D. L. Graphite Formation by Dissolution-Precipitation of Carbon in Nickel, Cobalt and Iron. *Carbon* **1975**, *13*, 111–113.
- (10) Oya, A.; Marsh, H. Phenomena of Catalytic Graphitization. *J. Mater. Sci.* **1982**, *17*, 309–322.
- (11) Moore, A. W. In *Chemistry and Physics of Carbon*; Walker, P. L., Thrower, P. A., Eds.; Marcel Dekker Inc.: New York, 1981; Vol. 17, p 233.
- (12) Krivoruchko, O. P.; Zaikovskii, V. I. A New Phenomenon Involving the Formation of Liquid Mobile Metal–Carbon Particles in the Low-Temperature Catalytic Graphitisation of Amorphous Carbon by Metallic Fe, Co and Ni. *Mendeleev Commun.* **1998**, *8*, 97–99.
- (13) Ni, L.; Kuroda, K.; Zhou, L.-P.; Ohta, K.; Matsuishi, K.; Nakamura, J. Decomposition of Metal Carbides as an Elementary Step of Carbon Nanotube Synthesis. *Carbon* **2009**, *47*, 3054–3062.
- (14) Sevilla, M.; Salinas Martínez-de Lecea, C.; Valdés-Solís, T.; Morallón, E.; Fuertes, A. B. Solid-Phase Synthesis of Graphitic Carbon Nanostructures from Iron and Cobalt Glucanates and Their Utilization as Electrocatalyst Supports. *Phys. Chem. Chem. Phys.* **2008**, *10*, 1433–1442.
- (15) Lee, K. T.; Ji, X.; Rault, M.; Nazar, L. F. Simple Synthesis of Graphitic Ordered Mesoporous Carbon Materials by a Solid-State Method Using Metal Phthalocyanines. *Angew. Chem., Int. Ed.* **2009**, *48*, 5661–5665.
- (16) Krivoruchko, O. P.; Shmakov, A. N.; Zaikovskii, V. I. In Situ X-ray Diffraction Study of Solid State Transformations During Catalytic Graphitisation of Amorphous Carbon. *Nucl. Instrum. Methods Phys. Rev.* **2001**, *470*, 198–201.
- (17) Anton, R. On The Reaction Kinetics of Ni With Amorphous Carbon. *Carbon* **2008**, *46*, 656–662.
- (18) Anton, R. In Situ TEM Investigations of Reactions of Ni, Fe and Fe–Ni Alloy Particles and Their Oxides with Amorphous Carbon. *Carbon* **2009**, *47*, 856–865.
- (19) Marsh, H.; Crawford, D.; Taylor, D. W. Catalytic Graphitization by Iron of Isotropic Carbon from Polyfurfuryl Alcohol, 725–1090 K. A High Resolution Electron Microscope Study. *Carbon* **1983**, *21*, 81–87.
- (20) Sevilla, M.; Fuertes, A. B. Catalytic Graphitization of Templated Mesoporous Carbons. *Carbon* **2006**, *44*, 468–473.
- (21) Lu, A. H.; Li, W. C.; Matoussevitch, N.; Spliethoff, B.; Bönneman, H.; Schüth, F. Highly Stable Carbon-Protected Cobalt Nanoparticles and Graphite Shell. *Chem. Commun.* **2005**, *1*, 98–100.
- (22) Lu, A. H.; Li, W. C.; Hao, G. P.; Spliethoff, B.; Bongerd, H. J.; Schaak, B. B.; Schüth, F. Easy Synthesis of Hollow Polymer, Carbon, and Graphitized Microspheres. *Angew. Chem., Int. Ed.* **2010**, *49*, 1615–1618.
- (23) Long, J. W.; Laskoski, M.; Peterson, G. W.; Keller, T. M.; Pettigrew, K. A.; Schindler, B. J. Metal-Catalyzed Graphitic Nanostructures as Sorbents for Vapor-Phase Ammonia. *J. Mater. Chem.* **2011**, *21*, 3477–3484.
- (24) Sevilla, M.; Sanchis, C.; Valdés-Solís, T.; Morallón, E.; Fuertes, A. B. Synthesis of Graphitic Carbon Nanostructures from Sawdust and Their Application as Electrocatalyst Supports. *J. Phys. Chem. C* **2007**, *111*, 9749–9756.
- (25) Thompson, E.; Danks, A. E.; Bourgeois, L.; Schnepf, Z. Iron-Catalyzed Graphitization of Biomass. *Green Chem.* **2015**, *117*, 551–556.
- (26) Sevilla, M.; Fuertes, A. B. Easy Synthesis of Graphitic Carbon Nanocoils from Saccharides. *Mater. Chem. Phys.* **2009**, *113*, 208–214.
- (27) Zhang, L.-S.; Li, W.; Cui, Z.-M.; Song, W.-G. Synthesis of Porous and Graphitic Carbon for Electrochemical Detection. *J. Phys. Chem. C* **2009**, *113*, 20594–20598.
- (28) Xie, M.; Yang, J.; Liang, J.; Guo, X.; Ding, W. In Situ Hydrothermal deposition as an Efficient Catalyst Supporting Method Towards Low-Temperature Graphitization of Amorphous Carbon. *Carbon* **2014**, *77*, 215–225.
- (29) Sevilla, M.; Sanchis, C.; Valdés-Solís, T.; Morallón, E.; Fuertes, A. B. Direct Synthesis of Graphitic Carbon Nanostructures from Saccharides and Their Use as Electrocatalytic Supports. *Carbon* **2008**, *46*, 931–939.
- (30) Herring, A. M.; McKinnon, J. T.; McCloskey, B. D.; Filley, J.; Gnesin, K. W.; Pavelka, R. A.; Kleebe, H. J.; Aldrich, D. J. A Novel Method for the Templated Synthesis of Homogeneous Samples of Hollow Carbon Nanospheres from Cellulose Chars. *J. Am. Chem. Soc.* **2003**, *125*, 9916–9917.
- (31) Sevilla, M.; Fuertes, A. B. Graphitic Carbon Nanostructures from Cellulose. *Chem. Phys. Lett.* **2010**, *490*, 63–68.
- (32) Glatzel, S.; Schnepf, Z.; Giordano, C. From Paper to Structured Carbon Electrodes by Inkjet Printing. *Angew. Chem., Int. Ed.* **2013**, *52*, 2355–2358.
- (33) Hoekstra, J.; Versluijs-Helder, M.; Vlietstra, E. J.; Geus, J. W.; Jenneskens, L. W. Carbon-Supported Base Metal Nanoparticles: Cellulose at Work. *ChemSusChem* **2015**, *8*, 985–989.
- (34) Sadezky, A.; Muckenhuber, H.; Grothe, H.; Niessner, R.; Pöschl, U. Raman Microspectroscopy of Soot and Related Carbonaceous Materials: Spectral Analysis and Structural Information. *Carbon* **2005**, *43*, 1731–1742.

- (35) Deck, C. P.; Vecchio, K. Prediction of Carbon Nanotube Growth Success by the Analysis of Carbon–Catalyst Binary Phase Diagrams. *Carbon* **2006**, *44*, 267–275.
- (36) Fujimoto, H. Theoretical X-ray Scattering Intensity of Carbons with Turbostratic Stacking and AB Stacking Structures. *Carbon* **2003**, *41*, 1585–1592.
- (37) Li, Z. Q.; Lu, C. J.; Xia, Z. P.; Zhou, Y.; Luo, Z. X-ray Diffraction Patterns of Graphite and Turbostratic Carbon. *Carbon* **2007**, *45*, 1686–1695.
- (38) Malard, L. M.; Pimenta, M. A.; Dresselhaus, G.; Dresselhaus, M. S. Raman Spectroscopy in Graphene. *Phys. Rep.* **2009**, *473*, 51–87.
- (39) Tuinstra, F.; Koenig, J. L. Raman Spectrum of Graphite. *J. Chem. Phys.* **1970**, *53*, 1126–1130.
- (40) Ferrari, A. C.; Robertson, J. Interpretation of Raman Spectra of Disordered and Amorphous Carbon. *J. Phys. Rev. B* **2000**, *61*, 14095.
- (41) Escribano, R.; Sloan, J. J.; Siddique, N.; Sze, N.; Dudev, T. Raman Spectroscopy of Carbon-Containing Particles. *Vib. Spectrosc.* **2001**, *26*, 179–186.
- (42) Sze, S. K.; Siddique, N.; Sloan, J. J.; Escribano, R. Raman Spectroscopic Characterization of Carbonaceous Aerosols. *Atmos. Environ.* **2001**, *35*, 561–568.
- (43) Gançado, L. G.; Pimenta, M. A.; Neves, B. R.; Dantas, M. S.; Joria, A. Influence of the Atomic Structure on the Raman Spectra of Graphite Edges. *Phys. Rev. Lett.* **2004**, *93*, 247401.
- (44) Cuesta, A.; Dhamelincourt, P.; Laureyns, J.; Martínez-Alonso, A.; Tascón, J. M. D. Raman Microprobe Studies on Carbon Materials. *Carbon* **1994**, *32*, 1523–1532.
- (45) Jawhari, T.; Roid, A.; Casado, J. Raman Spectroscopic Characterization of Some Commercially Available Carbon Black Materials. *Carbon* **1995**, *33*, 1561–1565.
- (46) Dipper, B.; Jander, H.; Heintzenberg, J. NIR FT Raman Spectroscopic Study of Flame Soot. *Phys. Chem. Chem. Phys.* **1999**, *1*, 4707–4712.
- (47) Lespade, P.; Marchand, A.; Couzi, M.; Cruege, F. Characterisation de Matériaux Carbones Par Microspectrométrie Raman. *Carbon* **1984**, *22*, 375–385.
- (48) Rhim, Y. R.; Zhang, D.; Rooney, M.; Nagle, D. C.; Fairbrother, D. H.; Herman, C.; Drewery, D. G. Changes in the Thermophysical Properties of Microcrystalline Cellulose as Function of Carbonization Temperature. *Carbon* **2010**, *48*, 31–40.
- (49) Rhim, Y. R.; Zhang, D.; Fairbrother, D. H.; Wepasnick, K. A.; Livi, K. J.; Bodnar, R. J.; Nagle, D. C. Changes in Electrical and Microstructural Properties of Microcrystalline Cellulose as Function of Carbonization Temperature. *Carbon* **2010**, *48*, 1012–1024.
- (50) Schaefer, Z. L.; Gross, M. L.; Hickner, M. A.; Schaak, R. E. Uniform Hollow Carbon Shells: Nanostructured Graphitic Supports for Improved Oxygen-Reduction Catalysis. *Angew. Chem., Int. Ed.* **2010**, *49*, 7045–7048.
- (51) Leng, Y.; Xie, F.; Liao, F.; Li, X. Kinetic and Thermodynamics Studies on the Decompositions of Ni_3C in Different Atmospheres. *Thermochim. Acta* **2008**, *473*, 14–18.
- (52) Linear thermal expansion coefficients of copper, nickel, cobalt, iron and graphite. http://www.kayelaby.npl.co.uk/general_physics/2_3/2_3_5.html (accessed Jan 9, 2015).
- (53) Saenger, K. L.; Tsang, J. C.; Bol, A. A.; Chu, J. O.; Grill, A.; Lavoie, C. In Situ X-ray Diffraction Study of Graphitic Carbon Formed During Heating and Cooling of Amorphous-C/Ni Bilayers. *Appl. Phys. Lett.* **2010**, *96*, 153105.
- (54) Ferrari, A. C. Raman Spectroscopy of Graphene and Graphite: Disorder, Electron-Phonon Coupling, Doping and Nonadiabatic Effects. *Solid State Commun.* **2007**, *143*, 47–57.
- (55) Gu, F.; Li, C.; Hu, Y.; Zhang, L. Synthesis and Optical Characterization of Co_3O_4 Nanocrystals. *J. Cryst. Growth* **2007**, *304*, 369–373.